The International Journal of Advanced Manufacturing Technology (2018) 99:2903–2913
https://doi.org/10.1007/s00170-018-2621-6

ORIGINAL ARTICLE

Influence of build layout and orientation on microstructural characteristics of electron beam melted Alloy 718

P. Karimi[1] · E. Sadeghi[1] · D. Deng[2] · H. Gruber[3] · J. Andersson[1] · P. Nylén[1]

Received: 7 January 2018 / Accepted: 19 August 2018 / Published online: 17 September 2018

Abstract
Effects of build layout and orientation consisting of (a) height from the build plate (Z-axis), (b) distance between samples, and (c) location in the build plate (X-Y plane) on porosity, NbC fraction, and hardness in electron beam melted (EBM) Alloy 718 were studied. The as-built samples predominantly showed columnar structure with strong <001> crystallographic orientation parallel to the build direction, as well as NbC and δ-phase in inter-dendrites and grain boundaries. These microstructural characteristics were correlated with the thermal history, specifically cooling rate, resulted from the build layout and orientation parameters. The hardness and NbC fraction of the samples increased around 6% and 116%, respectively, as the height increased from 2 to 45 mm. Moreover, by increasing the height, formation of δ-phase was also enhanced associated with lower cooling rate in the samples built with a greater distance from the build plate. However, the porosity fraction was unaffected. Increasing the sample gap from 2 to 10 mm did not change the NbC fraction and hardness; however, the porosity fraction increased by 94%. The sample location in the build chamber influenced the porosity fraction, particularly in interior and exterior areas of the build plate. The hardness and NbC fraction were not dependent on the sample location in the build chamber.

Keywords Additive manufacturing · Electron beam melting (EBM) · Alloy 718 · Hardness · Microstructural characterization

1 Introduction

Electron beam melting (EBM) is a powder-bed fusion additive-manufacturing (AM) technique which utilizes an electron beam as a heat source. The process is capable of producing geometrically complex parts with significant improvements in performance, weight and cost reduction, and an opportunity for design optimization [1–4]. Several studies have been performed to evaluate the microstructures and mechanical properties of EBM-manufactured Alloy 718 parts [5–8]. Moreover, the EBM process parameters such as beam power [9, 10], scanning speed [9, 11], and scanning strategy [12–14] have shown significant effects on microstructure and mechanical properties of Alloy 718. In the EBM-manufactured parts, the desired microstructure is affected by complex chemical and physical behavior of the melt pool as a result of non-equilibrium electron beam processing technique [1, 15]. There are, however, still challenges in the EBM manufacturing for high demanding industrial applications such as aerospace in terms of securing reproducibility, increasing build-up rate, anisotropy of mechanical properties [3, 16, 17], and controlling microstructure variations due to conditions within the build chamber.

In general, the EBM process parameters can be categorized into two main groups: (a) build layout and orientation which directly affect the thermal profile within the part being built, and (b) machine process parameters [18]. Build layout and orientation involve parameters such as sample design [3, 19], sample size [18], and building distance from the build plate [18], while machine process parameters include parameters such as scanning speed, beam current, focus offset, and line offset.

✉ P. Karimi
paria.karimi-neghlani@hv.se

[1] Department of Engineering Science, University West, 461 86 Trollhättan, Sweden

[2] Division of Engineering Materials, Department of Management and Engineering, Linköping University, 581 83 Linköping, Sweden

[3] Division of Materials and Manufacture, Industrial and Materials Science, University of Chalmers, 412 96 Gothenburg, Sweden

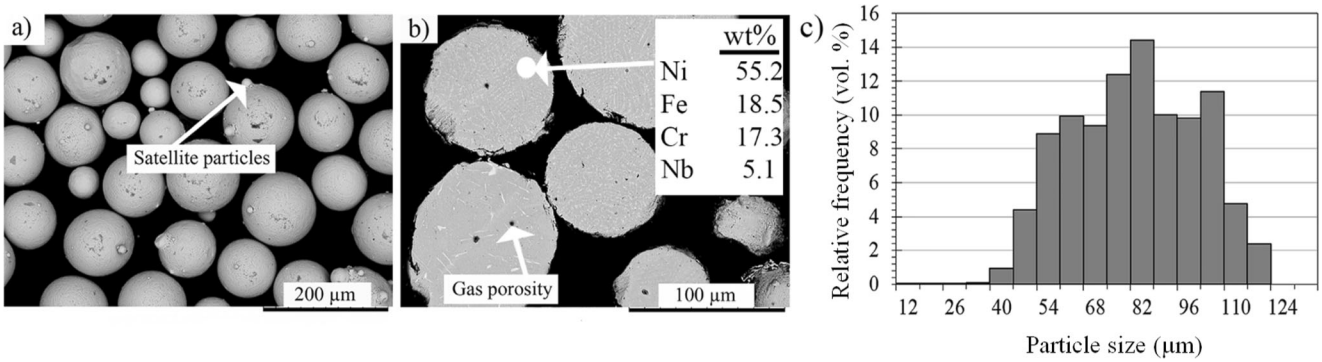

Fig. 1 Micrographs of the as-received Alloy 718 powder. **a** Secondary electron SEM image of the powder particles. **b** Back-scattered SEM image of cross-section of the powder and EDS analysis. **c** Size distribution of the powder

It can be assumed that by increasing the height from the build plate, grain structure and element segregation would be altered owing to the thermal mass/heat accumulation and change in the solidification condition. The gap between the samples in the build chamber can also be presumed to affect the microstructure. A smaller sample gap might increase the thermal mass/heat accumulation, which can lead to lower cooling rates, changes in grain orientation, and higher amount of element segregation. The location of the sample in the build chamber can be assumed to affect the microstructure. The interior of the build space is warmer, and the temperature radially decreases towards the exterior of the build space. It can therefore be expected that parts built in the exterior have a finer microstructure and higher hardness compared to parts built in the interior. The aim of this work was to verify these assumptions which to the author's knowledge, seem undoubtedly interested and important but have not been previously studied for Alloy 718 manufactured by the EBM process. Therefore, the present study was motivated to uncover the relationship between the build layout and orientation parameters and microstructural characteristics of the EBM-manufactured Alloy 718. The specific build layout and orientation parameters were (a) height from the build plate (Z-axis), (b) distance between the samples, and (c) sample location on the build plate (X-Y plane). The results of the present study provided information for tailoring the build layout and orientation parameters for desired microstructure and mechanical properties.

2 Materials and experimental work

2.1 Powder feedstock characterization

Plasma-atomized Alloy 718 powder supplied by Arcam AB, Sweden, was used as feedstock. The powder had a spherical shape with a few small satellite particles attached to the surface of big particles, as shown in Fig. 1a, b. The particle size of the feedstock powder was 45–105 µm (Fig. 1c). The chemical composition of the powder is given in Table 1.

2.2 Experimental setup

The building process was conducted under a controlled vacuum of 2×10^{-3} mbar with a small amount of helium in the build chamber and an acceleration voltage of 60 kV with an Arcam A2X EBM machine. The chamber temperature was kept at about 1025 °C measured by thermocouple beneath the build plate throughout the process. Six groups (groups A, B, C, D, E, and F) with different build layout and orientation parameters fabricated 62 cubic samples for the present study, as shown in Fig. 2. A 10-mm-thick build plate with the dimension of 170 × 170 mm of stainless steel was used. Groups A and B consisted of nine samples in a 3 × 3 matrix which had equal sample gap of 10 mm. While group A was built with a 2 mm height from the build plate and group B was directly built on the build plate, both groups were connected to the build plate using the support structure. Groups A and B from the build plate

Table 1 Chemical composition in wt% of Alloy 718 powder

Element	Ni	Co	Cr	Mo	Ti	Mn	Nb	B	P	Ta	Al	Fe	Si	S	C
wt%	54.11	0.04	19	2.99	1.02	0.12	4.97	0.001	0.004	< 0.01	0.12	Bal.	0.06	< 0.001	0.03

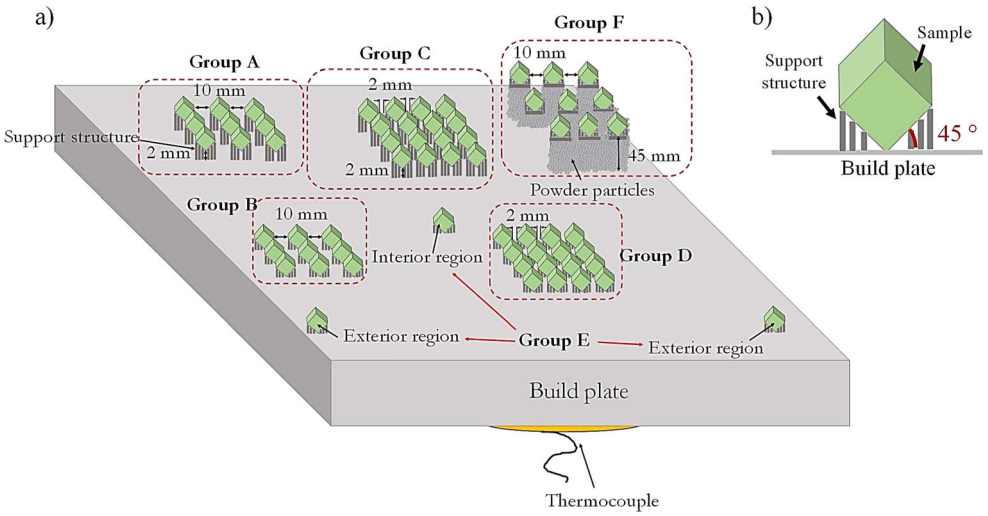

Fig. 2 **a** Schematic of EBM-manufactured Alloy 718 samples in different groups: A, B, C, D, E, and F. **b** The sample orientation on the build plate

were repeated for groups C and D (consisting of 4 × 4 matrix of samples each) which have the same height as groups A and B, respectively, but narrower sample gap (2 mm). In order to further analyze the effect of sample location in the chamber, group E was produced, having one cube in the interior area (E1) and two in the exterior area (E2 and E3). Furthermore, one additional group of cubic samples (F) with 3 × 3 matrix (sample gap 10 mm same as groups A and B) was produced at a 45-mm elevated position with respect to the build plate. These samples were built on the same support structure simply free floating on the powder bed and not connected to the build plate. Group F was produced using the same feedstock and same process conditions as the other groups, except a difference in distance from the build plate. Table 2 summarizes the layout and orientation parameters which had been used for different groups in Fig. 2. All samples had the same dimension of 10 × 10 × 10 mm and were built inclined around 45° on the build plate with the process parameters shown in Table 3 (Arcam standard theme for Alloy 718 in hatch and contour regions). The fabricated samples were investigated directly after EBM processing, without any subsequent post treatment.

2.3 Characterization of microstructure

The samples were cut from a normal reference plane parallel to the build direction (Fig. 3a), then grinded from 500 to 4000 grit and polished with diamond suspension and OP-U colloidal silica suspension. The polished samples were etched electrolytically using oxalic acid at room temperature with 6 V for 5 to 10 s. The microstructures of all samples were analyzed by light optical microscopy (LOM). For each sample, 16 images were taken at × 100 magnification to examine porosity and lack-of-fusion defects, based on point counting method presented in ASTM 562-08 [20].

A scanning electron microscope (SEM) (Hitachi TM3000, Tokyo, Japan) was used to characterize the microstructures. Energy dispersive spectroscopy (EDS) analysis was utilized to measure the chemical compositions of interested phases. Electron backscatter diffraction (EBSD) system (Oxford Instrument, Oxfordshire, UK) was employed to detail the crystallographic features, operating

Table 2 Layout and orientation parameters for different groups shown in Fig. 2

Group label	Height from build plate (mm)	Distance between samples (mm)	Sample location
A	2	10	–
B	0	10	–
C	2	2	–
D	0	2	–
E	–	–	Interior and exterior
F	45	10	–

Table 3 Main EBM process parameters (Arcam standard theme) used in manufacturing of Alloy 718

Parameter	Value
Layer thickness (μm)	75
Line offset (mm)	0.125
Speed function*	63
Scan strategy	Alternating ~ 60° in each layer

*Speed function index controls the scanning speed and beam current during process, and for each speed function value, the scanning speed and beam current adjust along the build direction

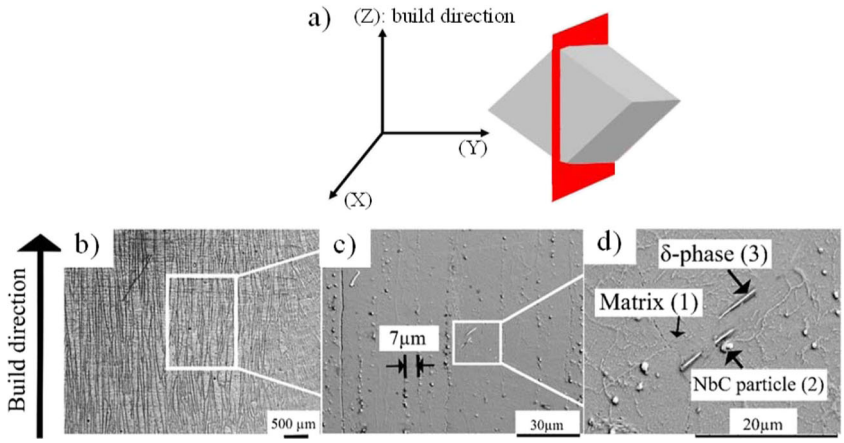

Fig. 3 **a** Sample cutting direction (Red plane) of the EBM-manufactured samples. **b** LOM image showed columnar grains. **c**, **d** SEM images illustrated MC particles and δ-phase

Table 4 Chemical composition (wt%) of the observed phases in Fig. 3c based on the EDS analysis

Precipitation composition	Ni	Cr	Fe	Al	Nb	Ti	Mo
Matrix (spectrum 1)	55.45	19.08	18.95	1.07	2.57	1.14	1.74
Carbide (spectrum 2)	6.1	3.4	2.3	–	78.4	9.8	–
δ-phase (spectrum 3)	69.12	1.72	2.12	0.88	23.91	2.25	–

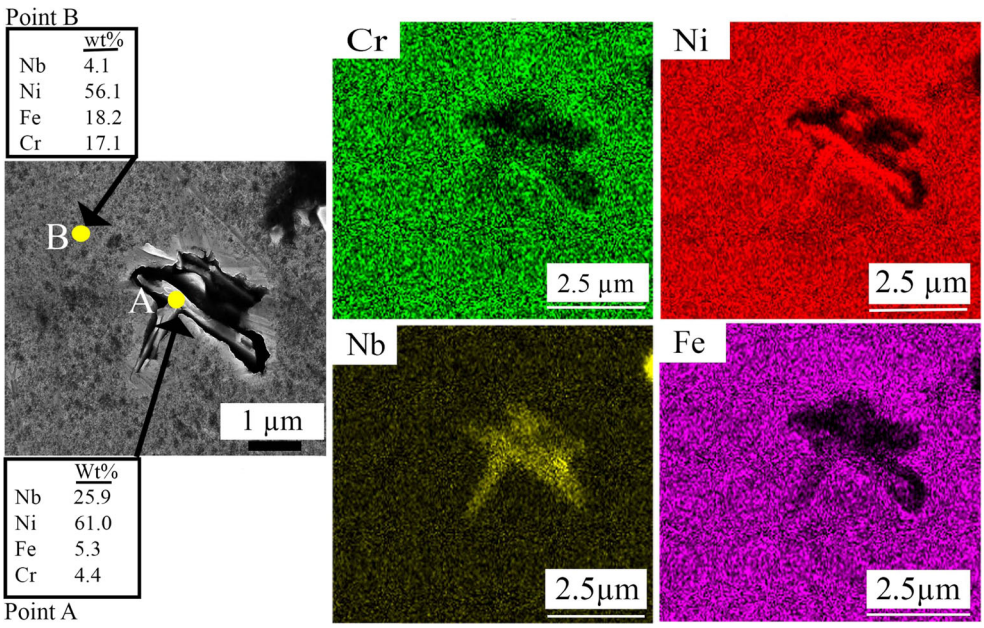

Fig. 4 Back-scattered SEM image with EDS composition maps showing concentration of Ni, Cr, Fe, and Nb in the δ-phase

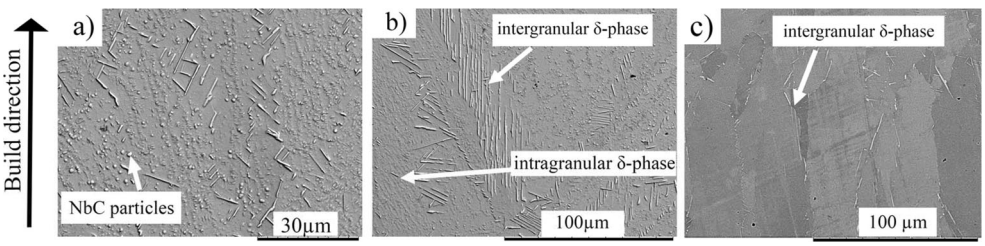

Fig. 5 **a**, **b** SEM images from the etched surface. **c** SEM image before etching the surface, showing δ-phase distribution at grain boundaries in the samples with 45 mm height from the build plate (group F)

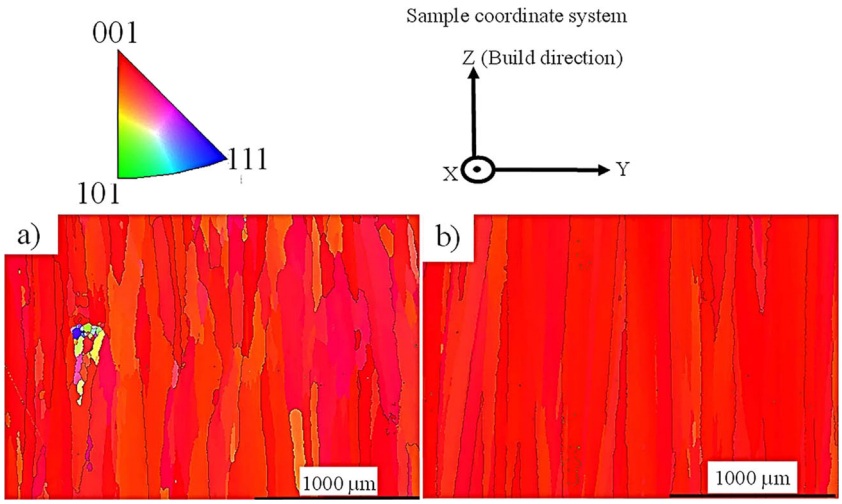

Fig. 6 EBSD orientation maps in parallel to the build direction (YZ plane). **a** Sample B4, with 0 mm height from the build plate. **b** Sample F4, sample with 45 mm height from the build plate

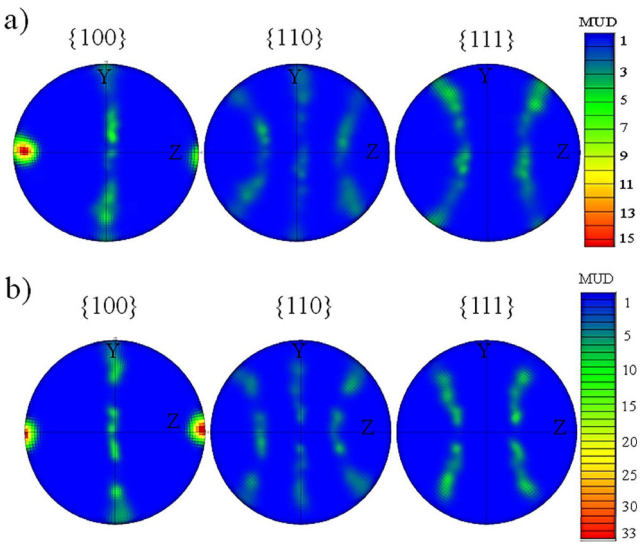

Fig. 7 Representative pole figures in the YZ plane. **a** Columnar grains in sample B4 built on 0 mm height from the build plate. **b** Well-oriented columnar grains in sample F4 built on 45 mm height from the build plate

at 20 kV of accelerating voltage and with step size of 2 µm. Vickers microhardness (HV) measurements were performed using a hardness tester (HMV-2, Shimadzu, Kyoto, Japan) by an applied load of 500 g and a dwell time of 15 s. In order to get good statistics, ten hardness indentations were performed for each sample.

3 Results and discussion

3.1 Microstructures of the EBM samples in all groups

As shown in Fig. 3b, the grains were mainly columnar and elongated along the build direction. Precipitates can be found align inter-dendritically along the build direction and chain up (see Fig. 3c). Within the columnar region, the primary dendrite arm spacing (PDAS) was ~ 6–10 µm (Fig. 3c). Based on the relationship between experimentally derived cooling rate and PDAS in Eq. (1), a cooling rate of 1000–7000 K/s was estimated [7, 21–24].

$$\lambda = A\,\dot{T}^{-n} \tag{1}$$

where λ is the primary dendrite arm spacing, $\dot{T}$ is cooling rate, and A and n are proportionality coefficients.

The EDS analysis taken from the points in Fig. 3d (presented in Table 4) confirmed with the EDS elemental mapping in Fig. 4, showing the presence of the γ-phase matrix (point 1), precipitation of round/square shape MC carbides (point 2), probably NbC or TiC with less than 2 µm size, and plate-like shape δ-phase precipitation with Ni_3Nb chemical composition (point 3). A similar founding regarding the microstructure was also reported in the literature [13–15].

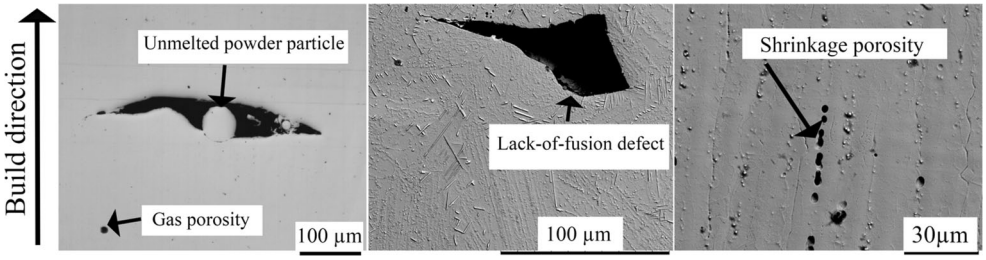

Fig. 8 **a** LOM image of gas porosity and lack-of-fusion defect in sample C3. **b** SEM image of lack-of-fusion defect in sample D5. **c** SEM image of agglomerated shrinkage porosity in sample C16

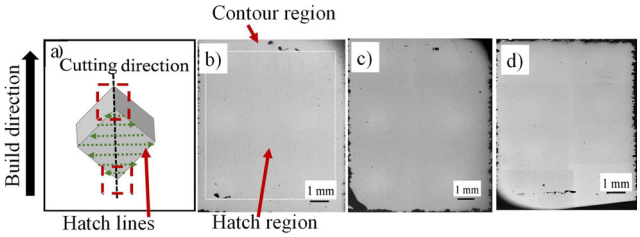

Fig. 9 **a** Red hatched square representative of shorter hatch lines, and LOM images representative of overall surface of sample YZ plane in different process conditions. **b** Sample A5: 2 mm height from the build plate. **c** Sample B5: 0 mm height from the build plate. **d** Sample F5: 45 mm height from the build plate

Comparing most of the EBM groups (A, B, C, D, and E) based on the SEM analysis of the secondary phases, there were no significant differences with regard to amount of the δ-phase. However, the δ-phase in group F was more in content and longer in length than the other groups, which can be due to a quite different thermal history (group F had the height of 45 mm from the build plate). By reason of lower thermal conductivity of powder, the samples in group F stayed a long time within the δ-phase precipitation zone, which is about 870–1010 °C, than other groups (A, B, C, D, and E), and therefore had more δ-phase [25–28]. As shown in Fig. 5, the platelets of δ-phase were more elongated in group F compared to the other groups (see Fig. 3d). In Fig. 5b, c, the δ-phase precipitates were organized in clusters of elongated parallel plates in intergranular areas, whereas intragranular δ-phase was in small size. In addition, the intergranular δ-phase was brighter than the intragranular ones due to its larger content of Nb. Presumably, the δ-phase started its precipitation at the grain boundaries; however, as the temperature or dwell time increased (lower cooling rate ~ 300 K/s), the intragranular δ-phase precipitates can appear [29], as shown in Fig. 5b.

3.2 Effect of build layout and orientation parameters on secondary phase constituents, porosity, and hardness

3.2.1 Effect of height from build plate

The EBSD orientation maps (IPF-maps) and pole figures (PFs) in Figs. 6 and 7 show the effect of height from the build plate on the grain structure. The microstructure exhibited a high degree of texture, namely the <001> crystallographic orientation aligned parallel to the build direction. As discussed previously, this result is typical for the AM processes [9, 13, 14, 30, 31]. Although the strong columnar structure was shown in the samples built on the build plate as well as the ones built 2 mm from the build plate in Fig. 6a, the emergence of some stray grains demonstrated that nucleation of new grains ahead of the solidification front was accelerated. Formation of the stray grain led to lower grain width for the samples in groups A and B. The tendency for formation of the

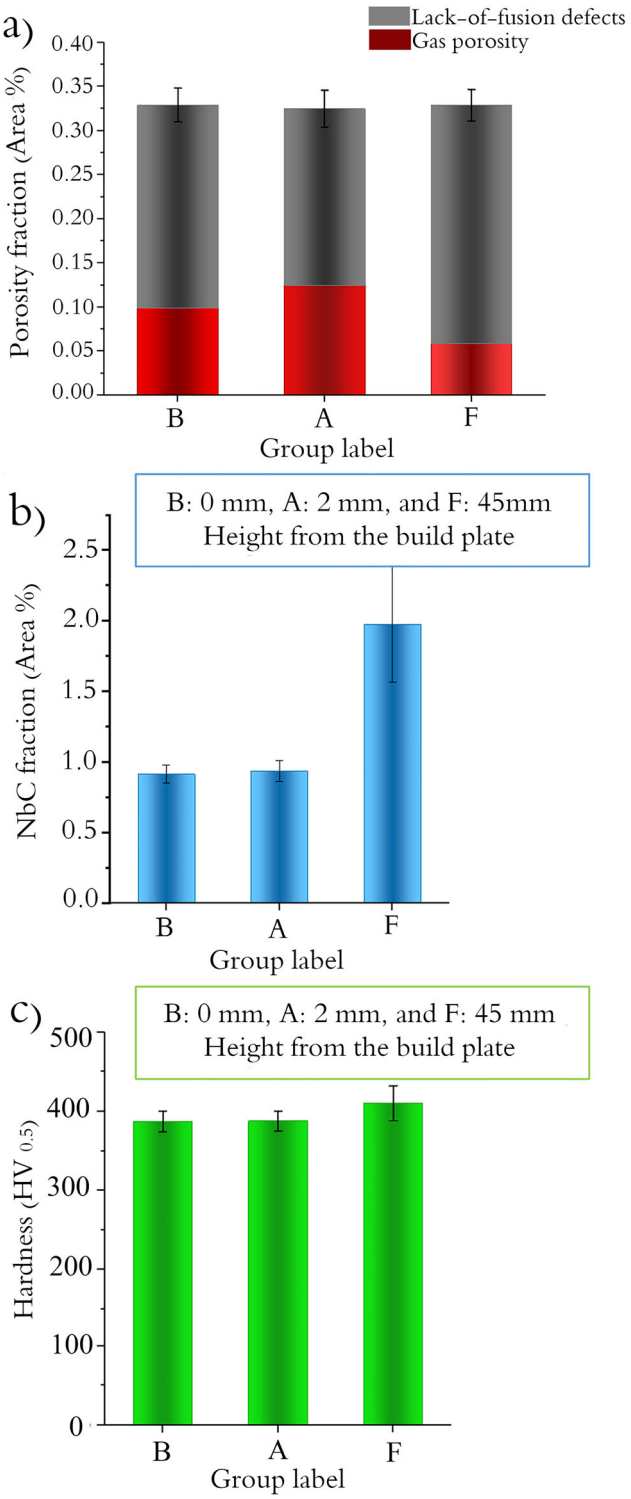

Fig. 10 Effect of height from the build plate on **a** porosity fraction, **b** NbC fraction, and **c** hardness of EBM-manufactured Alloy 718 samples in groups B, 0; A, 2; and F, 45 mm

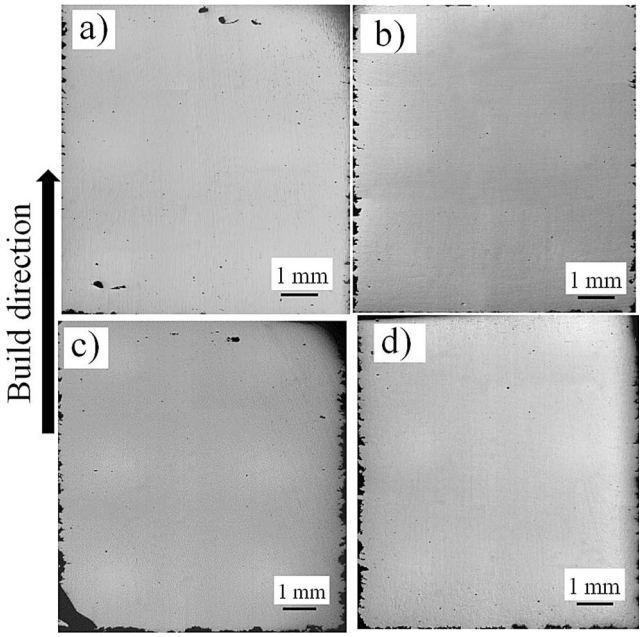

Fig. 11 LOM images representative of overall surface of sample YZ plane in different process conditions. **a** Sample A5: 10 mm sample gap (2 mm building height). **b** Sample C10: 2 mm sample gap (2 mm building height). **c** Sample B5: 10 mm sample gap (0 mm building height). **d** Sample D10: 2 mm sample gap (0 mm building height)

new stray grains in the samples of groups A and B can be most likely attributed to:

i. A slightly higher cooling rate in lower height from the build plate due to faster heat conduction to the build plate [32],
ii. Un-melted powder particles in lack-of-fusion defects as initiation sites for fragmentation of dendrites which were coming from previous layers and stray grain nucleation [33].

In contrast, the elevated samples from the build plate disclosed a more predominant columnar grain structure as shown in Fig. 6b. PFs in Fig. 7a also confirmed lower multiple of uniform density (MUD) of maximum 15.56 in samples built on the build plate, while PFs in Fig. 7b for samples with 45 mm height from the build plate exhibited the maximum MUD of 34.39 as it showed a strong texture in the build direction.

It has been shown that porosity, both gas pores and lack-of-fusion defects, which can be influenced by the build layout and orientation parameters as well as machine process parameters, adversely affect the mechanical properties [34]. For instance, tensile strength can be altered by changing the build layout and orientation parameters such as sample location and sample height [35]. OM and SEM images of gas porosity, lack-of-fusion defects, and local agglomerated shrinkage pores in the different process conditions are shown in Fig. 8a–c. Large cavities filled with or without loosely held un-melted powder particles shown in Fig. 8a, b can be a result of the localized low energy input, which caused small melt pool depth. As a result, the powder particles were not fully melted to form strong bonding between the layers [36, 37]. The shrinkage pores were

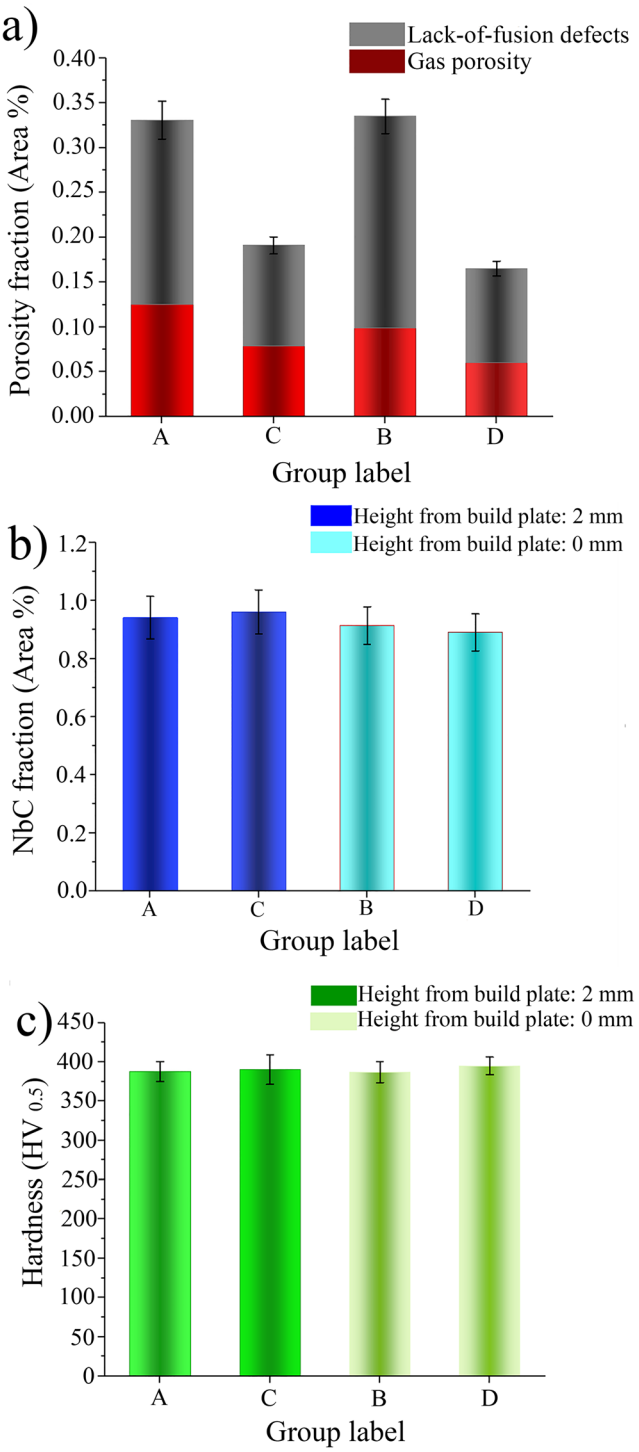

Fig. 12 Effect of distances between samples on **a** porosity fraction, **b** NbC fraction, and **c** hardness of EBM-manufactured Alloy 718 samples in groups A, 10; C, 2; B, 10; and D, 2 mm

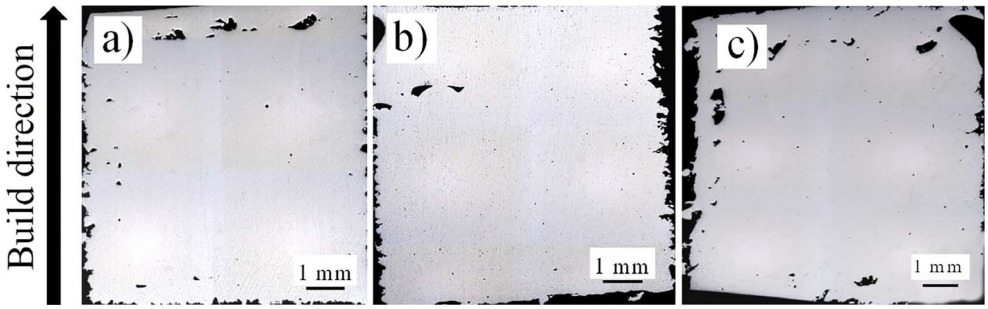

Fig. 13 LOM images of overall surface of sample YZ plane in different process conditions. **a** E1: interior sample. **b** E2: exterior sample. **c** E3: exterior sample

arranged in strings parallel to the build direction (see Fig. 8c), probably originated from a former dendrite microstructure [5]. In addition, these pores aligning along the MC precipitates can be observed in some locations, indicating that the shrinkage porosity probably formed in the inter-dendritic region which is the last area to solidify [38].

Figure 9 shows a general view of the distribution of the pores in YZ plane parallel to the build direction. More and larger pores were more likely to be found in both top and bottom areas of all samples which were due to shorter hatch lines (showed by a red hatched square). As shown in Fig. 9a, not only the length of the hatch scan was short in the beginning and end of the building process (mainly attributed to the contour region), but also spot melting strategy (typically implemented for the contour region) was used to build these areas (see Fig. 9b). The occurrence of these two phenomena led to formation of more and larger pores at the top and bottom of the samples. But in general, the porosity fraction was shown similar in the samples with 0, 2, and 45 mm heights from the build plate (see Fig. 10a). Due to a high thermal mass (as a result of having powder particles under the samples), the elevated samples in group F with high distance from the build plate (45 mm) were expected to be less porous than the samples in groups A and B. However, the porosity fraction was almost similar in all the three groups. To explain this, it should be mentioned that the temperature of the melt pool in the samples is affected by the thermal conductivity of the powder beneath the samples. A high amount of powder beneath the samples in group F increased the thermal mass/heat accumulation and led to formation of a high temperature melt pool with low stability and vigorous motion. This phenomenon probably promoted formation of more voids and pores during solidification in group F [39, 40]. As shown in Fig. 10b, the samples in groups A and B had almost the same amount of NbC, which accounted for only half of that in group F. It could be attributed to the lower thermal conductivity of the powder leading to lower heat conduction to the build plate which acted as a heat sink for samples built on the build plate. Therefore, the available time for Nb segregation for group F was increased in comparison to groups A and B. Similar to the trend of NbC fraction, the hardness of the samples in groups A and B was almost the same, but slightly lower than group F (see Fig. 10c). It could be due to either the cooling condition of group F once the building job finished, was more favorable for precipitating gamma double prime than groups A and B, or grain boundary hardening by precipitation of inter-granular δ-phase at grain boundaries which avoid grain coarsening [23].

3.2.2 Effect of distances between samples

It is also of interest to investigate how the distance between the samples with the same building heights affected the microstructure. It should be noted that groups A and C had the same build height (2 mm) but different sample gaps (10 and 2 mm, respectively), and also groups B and D were built with a same build height (0 mm) but different sample gaps (10 and 2 mm, respectively). As shown in Fig. 11, pores in the top and bottom of the samples were clearly visible; however, in general, the overview of the YZ plane revealed a lower amount of porosity in the samples with smaller sample gaps (groups C and D). The porosity fraction was measured and compared for the different sample gaps in Fig. 12a. It was shown that by increasing the sample gap from 2 mm (the minimum recommended value by the EBM machine manufacturer) to 10 mm, the amount of porosity was increase around 94%. The reason attributed to the higher thermal mass/heat accumulation in lower sample gaps which induce less amount of unmelted powder particles for pore formation. Higher sample gaps had lower thermal mass/heat accumulation compared to lower sample gaps which might be a reason for involving less powder particles during melting process, leading to more porous microstructures.

According to Fig. 12b, by decreasing the sample gap, thermal mass/heat accumulation is expected to increase, and thus cooling rate decrease, which implies an increase in the NbC fraction. However, no results confirmed this hypothesis since there were negligible differences between these groups. The result from the hardness measurements for different sample gaps is given in Fig. 12c. In this comparison between these groups ((A, C) and (B, D)), no significant differences were revealed. The reason might be that a larger difference in sample gaps would have been needed to see the changes of NbC fraction and hardness.

3.2.3 Effect of sample location

Figure 13 shows large lack-of-fusion defects mainly in the top and bottom of the samples. In general, the samples in group E had higher amount of pores than the other groups which can be attributed to their positions. The samples in group E had arrangement as single samples, whereas the other samples were designed in groups (for instance, 9 samples in group A). The lower thermal mass/heat accumulation in group E due to the single arrangement led to formation of more pores. E3, which was built in the exterior area, showed a higher amount of porosity fraction than E1, which was positioned in the interior area of the build plate. However, E2 in the exterior area contradicted the results of E3 by having a lower amount of total porosity (see Fig. 14a). The exact reason remains unknown as further investigation is needed.

Furthermore, as shown in Fig. 14b, c, no significant differences were obtained in the NbC fraction and hardness between E1, E2, and E3. However, to clearly explain the effect of sample location on microstructural characteristics, more investigations are needed.

4 Conclusions

The EBM technique was used to build different groups of samples from Alloy 718 powder and to investigate the effect of three build layout and orientation parameters including (a) height from the build plate, (b) sample gap, and (c) sample location in the build chamber on the microstructure and hardness. Characterization of microstructural features illustrates a number of findings which are usefully summarized as follows:

- Columnar grains with strong texture of <001> crystallographic orientation parallel to the build direction as well as precipitation of NbC and δ-phase in inter-dendrites and grain boundaries were observed.
- Increasing the distance from the build plate led to the formation of predominant columnar microstructure. The stray grains were found less in the samples built with the higher height from the build plate.
- By increasing the height to 45 mm from the build plate, formation of δ-phase was enhanced as well as the NbC fraction increased about 116% and hardness slightly increased around 6%, but the porosity fraction was shown not to vary significantly.
- By increasing the sample gap (from 2 to 10 mm), no significant effect was found on the NbC fraction and hardness, but in the larger sample gap, the porosity fraction was increased about 94%.

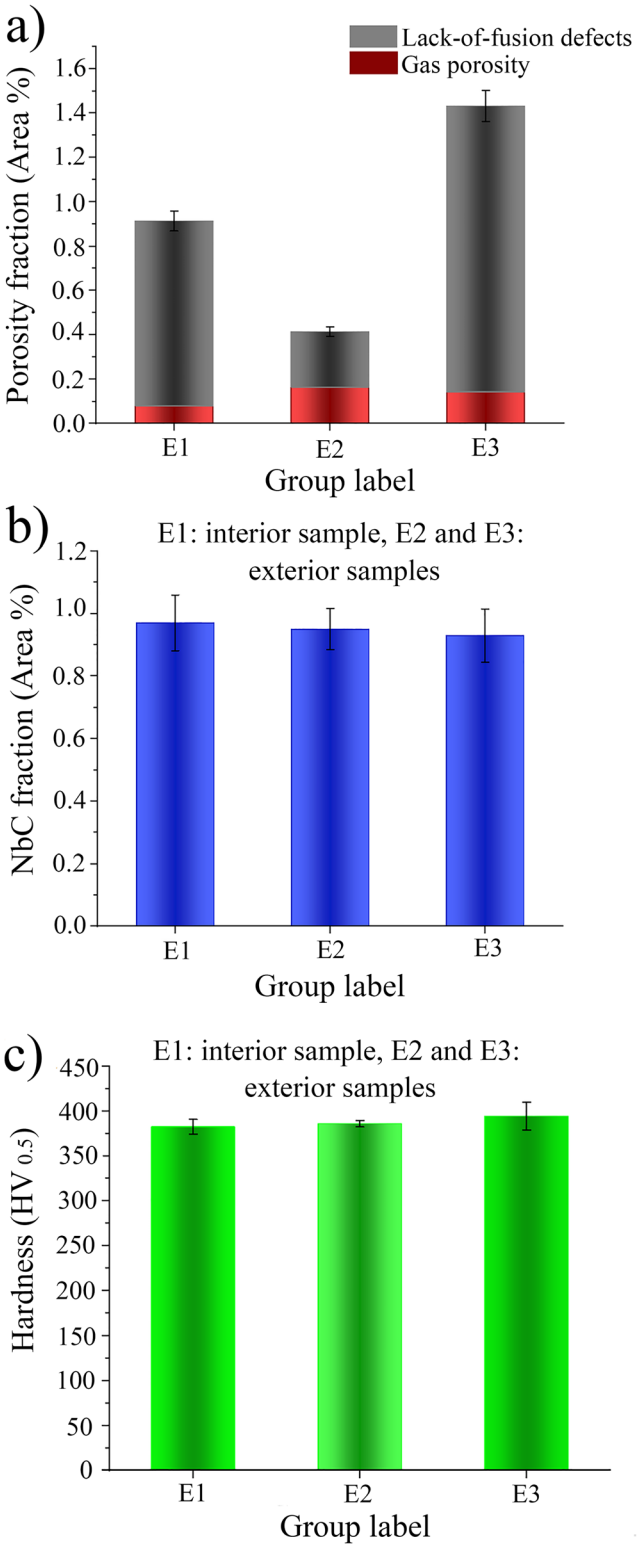

Fig. 14 Effect of sample location on **a** porosity fraction, **b** NbC fraction, and **c** hardness of EBM-manufactured Alloy 718 samples; E1: interior sample, E2: exterior sample, and E3: exterior sample

- The effect of sample location on the porosity was evident in which the former decreased in the exterior sample while the latter increased; however, its effect on NbC fraction and hardness was insignificant.

Acknowledgments The authors would like to thank Mr. Anders Snis, and Mr. Jonas Olsson for sharing their knowledge in running the EBM machine and material preparation.

Funding information The funding from the European Regional Development Fund, as well as Simulation and Control of Material affecting Processes (SiCoMap) research group, and KK foundation is acknowledged.

References

1. Sames WJ, Unocic KA, Dehoff RR, Lolla T, Babu SS (2014) Thermal effects on microstructural heterogeneity of Inconel 718 materials fabricated by electron beam melting. J Mater Res 29(17):1920–1930
2. Kirka MM, Medina F, Dehoff R, Okello A (2017) Mechanical behavior of post-processed Inconel 718 manufactured through the electron beam melting process. Mater Sci Eng A 680:338–346
3. Al-Bermani SS, Blackmore ML, Zhang W, Todd I (2010) The origin of microstructural diversity, texture, and mechanical properties in electron beam melted Ti-6Al-4V. Metall Mater Trans A 41(13):3422–3434
4. Murr LE, Gaytan SM, Martinez E, Medina FR (2012) Metal fabrication by additive manufacturing using laser and electron beam melting technologies. J Mater Sci Technol 28(1):1–14
5. Strondl A, Palm M, Gnauk J, Frommeyer G (2011) Microstructure and mechanical properties of nickel based superalloy IN718 produced by rapid prototyping with electron beam melting (EBM). Mater Sci Technol 27(5):876–883
6. Cakmak E, Watkins TR, Bunn JR, Cooper RC, Cornwell PA, Wang Y, Sochalski-Kolbus LM, Dehoff RR, Babu SS (2016) Mechanical characterization of an additively manufactured Inconel 718 theta-shaped specimen. Metall Mater Trans A 47(2):971–980
7. Kirka MM, Unocic KA, Raghavan N, Medina F, Dehoff RR, Babu SS (2016) Microstructure development in electron beam-melted Inconel 718 and associated tensile properties. JOM 68(3):1012–1020
8. Strondl A, Fischer R, Frommeyer G, Schneider A (2008) Investigations of MX and γ'/γ'' precipitates in the nickel-based superalloy 718 produced by electron beam melting. Mater Sci Eng A 480(1–2):138–147
9. Helmer HE, Körner C, Singer RF (2014) Additive manufacturing of nickel-based superalloy Inconel 718 by selective electron beam melting: processing window and microstructure. J Mater Res 29(17):1987–1996
10. Raghavan N et al (2016) Numerical modeling of heat-transfer and the influence of process parameters on tailoring the grain morphology of IN718 in electron beam additive manufacturing. Acta Mater 112(Supplement C):303–314
11. Price S, Cheng B, Lydon J, Cooper K, Chou K (2014) On process temperature in powder-bed electron beam additive manufacturing: process parameter effects. J Manuf Sci Eng 136(6):061019–061019–10
12. Helmer H, Bauereiß A, Singer RF, Körner C (2016) Grain structure evolution in Inconel 718 during selective electron beam melting. Mater Sci Eng A 668(Supplement C):180–187
13. Dehoff RR, Kirka MM, List FA, Unocic KA, Sames WJ (2015) Crystallographic texture engineering through novel melt strategies via electron beam melting: Inconel 718. Mater Sci Technol 31(8):939–944
14. Kirka MM, Lee Y, Greeley DA, Okello A, Dehoff RR (2017) Strategy for texture management in metals additive manufacturing. JOM 69(3):523–531
15. Kirka MM, Nandwana P, Lee Y, Dehoff RR (2017) Solidification and solid-state transformation sciences in metals additive manufacturing. Scr Mater 135(Supplement C):130–134
16. Antonysamy AA, Prangnell PB, Meyer J (2012) Effect of wall thickness transitions on texture and grain structure in additive layer manufacture (ALM) of Ti-6Al-4V. Mater Sci Forum 706–709:205–210
17. Wang F, Williams S, Colegrove P, Antonysamy AA (2013) Microstructure and mechanical properties of wire and arc additive manufactured Ti-6Al-4V. Metall Mater Trans A 44(2):968–977
18. Hrabe N, Quinn T (2013) Effects of processing on microstructure and mechanical properties of a titanium alloy (Ti–6Al–4V) fabricated using electron beam melting (EBM), part 2: energy input, orientation, and location. Mater Sci Eng A 573:271–277
19. Svensson M Ackelid U (2009) Additive manufacturing of dense metal parts by electron beam melting - Heat Treating Society
20. ASTM E562-08 (2008) Standard test method for determining volume fraction by systematic manual point count. ASTM International, West Conshohocken www.astm.org
21. Tien JK, Caulfield T (1989) Superalloys, supercomposites, and superceramics. Academic Press, Boston
22. Kurz W, Giovanola B, Trivedi R (1986) Theory of microstructural development during rapid solidification. Acta Metall 34(5):823–830
23. Zhang Y, Li Z, Nie P, Wu Y (2013) Effect of cooling rate on the microstructure of laser-remelted INCONEL 718 coating. Metall Mater Trans A 44(12):5513–5521
24. Tien JK (2012) Superalloys, supercomposites, and superceramics. Elsevier
25. Gong X, Wang X, Cole V, Jones Z, Cooper K, Chou K (2015) Characterization of microstructure and mechanical property of Inconel 718 from selective laser melting, in ASME 2015 International Manufacturing Science and Engineering Conference, p. V001T02A061–V001T02A061
26. CT Sims, NS Stoloff, WC Hagel (1987) Wiley: superalloys II: high-temperature materials for aerospace and industrial power - Chester T. Sims, Norman S. Stoloff, William C. Hagel
27. Sundararaman M, Mukhopadhyay P, Banerjee S (1992) Some aspects of the precipitation of metastable intermetallic phases in INCONEL 718. Metall Trans A 23(7):2015–2028
28. Kirman I, Warrington DH (1970) The precipitation of Ni3Nb phases in a Ni–Fe–Cr–Nb alloy. Metall Trans A 1(10):2667–2675
29. Mahadevan S, Nalawade S, Singh JB, Verma A, Paul B, Ramaswamy K (2010) Evolution of δ phase microstructure in alloy 718. In: Ott EA, Groh JR, Banik A, Dempster I, Gabb TP, Helmink R, Liu X, Mitchell A, Sjöberg GP, Wusatowska-Sarnek A (eds) Superalloy 718 and derivatives. Wiley, Hoboken, pp 737–750
30. Sames W (2015) Additive manufacturing of Inconel 718 using electron beam melting: processing, post-processing, & mechanical properties, Thesis

31. Karimi P, Raza T, Andersson J, Svensson L-E (2017) Influence of laser exposure time and point distance on 75-μm-thick layer of selective laser melted Alloy 718. Int J Adv Manuf Technol 94:1–9
32. Pryds NH, Huang X (2000) The effect of cooling rate on the microstructures formed during solidification of ferritic steel. Metall Mater Trans A 31(12):3155–3166
33. Dehoff RR, Kirka MM, Sames WJ, Bilheux H, Tremsin AS (2015) Site specific control of crystallographic grain orientation through electron beam additive manufacturing. Mater Sci Technol 31(8): 931–938
34. Tammas-Williams S, Withers PJ, Todd I, Prangnell PB (2017) The influence of porosity on fatigue crack initiation in additively manufactured titanium components. Sci Rep 7(1):7308
35. Galarraga H, Lados DA, Dehoff RR, Kirka MM, Nandwana P (2016) Effects of the microstructure and porosity on properties of Ti-6Al-4V ELI alloy fabricated by electron beam melting (EBM). Addit Manuf 10:47–57
36. Bontha S, Klingbeil NW, Kobryn PA, Fraser HL (2009) Effects of process variables and size-scale on solidification microstructure in beam-based fabrication of bulky 3D structures. Mater Sci Eng A 513–514:311–318
37. Joy Gockel JB (2013) Publication: understanding Ti-6Al-4V microstructure control in additive manufacturing via process maps
38. Strondl A (2010) Characterisation of nickel-based superalloys manufactued by electron beam melting, Doctoral thesis, Chalmers University of Technology
39. Xia M, Gu D, Yu G, Dai D, Chen H, Shi Q (2017) Porosity evolution and its thermodynamic mechanism of randomly packed powder-bed during selective laser melting of Inconel 718 alloy. Int J Mach Tools Manuf 116:96–106
40. Nm LL, Ndop J, Jm B (2017) Investigations of thermal damage on the physical and mechanical properties of gneiss rock specimen. J Powder Metall Min 6(3):1–6